

This work was written as part of one of the author's official duties as an Employee of the United States Government and is therefore a work of the United States Government. In accordance with 17 U.S.C. 105, no copyright protection is available for such works under U.S. Law. Access to this work was provided by the University of Maryland, Baltimore County (UMBC) ScholarWorks@UMBC digital repository on the Maryland Shared Open Access (MD-SOAR) platform.

Please provide feedback

Please support the ScholarWorks@UMBC repository by emailing scholarworks-group@umbc.edu and telling us what having access to this work means to you and why it's important to you. Thank you.



Vertical Dependence of Horizontal Variation of Cloud Microphysics: Observations from the ACE-ENA field campaign and implications for warm rain simulation in climate models

5 Zhibo Zhang^{1,2,*}, Qianqian Song^{1,2}, David B. Mechem³, Vincent E. Larson⁴, Jian Wang⁵,
Yangang Liu⁶, Mikael K. Witte^{7,8}, Xiquan Dong⁹, Peng Wu^{9,10}

1. Physics Department, University of Maryland Baltimore County (UMBC), Baltimore,
21250, USA
- 10 2. Joint Center for Earth Systems Technology, UMBC, Baltimore, 21250, USA
3. Department of Geography and Atmospheric Science, University of Kansas, Lawrence,
66045, USA
4. Department of Mathematical Sciences, University of Wisconsin — Milwaukee,
Milwaukee, 53201, USA
- 15 5. Center for Aerosol Science and Engineering, Department of Energy, Environmental and
Chemical Engineering, Washington University in St. Louis, St. Louis, 63130, USA
6. Environmental and Climate Science Department, Brookhaven National Laboratory,
Upton, 11973, USA
- 20 7. Joint Institute for Regional Earth System Science and Engineering, University of
California Los Angeles, Los Angeles, 90095, USA
8. Jet Propulsion Laboratory, California Institute of Technology, Pasadena, 91011, USA
9. Department of Hydrology and Atmospheric Sciences, University of Arizona, Tucson,
85721, USA
10. Pacific Northwest National Laboratory, Richland, WA 99354, USA

25 To be submitted to the ACP special issue: Marine aerosols, trace gases, and clouds over the
North Atlantic

Correspondence to: Zhibo Zhang (zhibo.zhang@umbc.edu)



Abstract:

In the current global climate models (GCM), the nonlinearity effect of subgrid cloud variations on the parameterization of warm rain process, e.g., the autoconversion rate, is often treated by multiplying the resolved-scale warm rain process rates by a so-called enhancement factor (EF). In this study, we investigate the subgrid-scale horizontal variations and covariation of cloud water content (q_c) and cloud droplet number concentration (N_c) in marine boundary layer (MBL) clouds based on the in-situ measurements from a recent field campaign, and study the implications for the autoconversion rate EF in GCMs. Based on a few carefully selected cases from the field campaign, we found that in contrast to the enhancing effect of q_c and N_c variations that tends to make $EF > 1$, the strong positive correlation between q_c and N_c results in a suppressing effect that makes tends to make $EF < 1$. This effect is especially strong at cloud top where the q_c and N_c correlation can be as high as 0.95. We also found that the physically complete EF that accounts for the covariation of q_c and N_c has a robust decreasing trend from cloud base to cloud top. Because the autoconversion process is most important at the cloud top, this vertical dependence of EF should be taken into consideration in the GCM parametrization scheme.



48

49 1. Introduction

50 Marine boundary layer (MBL) clouds cover about 1/5 of Earth's surface and play an important
 51 role the climate system (*Wood, 2012*). A faithful simulation of MBL clouds in the global climate
 52 model (GCM) is critical for the projection of future climate (*Bony and Dufresne, 2005; Bony et*
 53 *al., 2015; Boucher et al., 2013*) and understanding of aerosol-cloud interactions (*Carslaw et al.,*
 54 *2013; Lohmann and Feichter, 2005*). Unfortunately, it turns out to be an extremely challenging
 55 task. Among others, an important reason is that many physical processes in MBL clouds occur at
 56 the spatial scales much smaller than the typical resolution of GCMs, making the simulation of
 57 these processes in GCMs highly challenging.

58 Of particular interest in this study is the warm rain process that play an important role in
 59 regulating the lifetime, water budget, and therefore integrated radiative effects of MBL clouds. In
 60 the bulk cloud microphysics schemes that are widely used in GCMs (*Morrison and Gettelman,*
 61 *2008*), continuous cloud particle spectrum is often divided into two modes. Droplets smaller than
 62 the "separation size" r^* are classified into the cloud mode, which is described by two moments of
 63 droplet size distribution (DSD), the droplet number concentration N_c (0th moment of DSD) and
 64 droplet liquid water content q_c (proportional to the 3rd moment). Droplets larger than r^* are
 65 classified into a precipitation mode (drizzle or rain), with properties denoted by drop concentration
 66 and water content (N_r and q_r). In a bulk microphysics scheme, the transfer of mass from the cloud
 67 to rain modes as a result of the collision-coalescence process is separated into two terms,
 68 autoconversion and accretion: $\left(\frac{\partial q_r}{\partial t}\right)_{coal} = \left(\frac{\partial q_r}{\partial t}\right)_{auto} + \left(\frac{\partial q_r}{\partial t}\right)_{acc}$. Autoconversion is defined as the
 69 rate of mass transfer from the cloud to rain mode due to the coalescence of two cloud droplets with
 70 $r < r^*$. Accretion is defined as the rate of mass transfer due to the coalescence of a rain drop with



71 $r > r^*$ with a cloud droplet. A number of autoconversion and accretion parameterizations have
 72 been developed, formulated either through numerical fitting of droplet spectra obtained from bin
 73 microphysics LES or parcel model (*Khairoutdinov and Kogan, 2000*), or through an analytical
 74 simplification of the collection kernel to arrive at expressions that link autoconversion and
 75 accretion with the bulk microphysical variables (*Liu and Daum, 2004*). For example, a widely used
 76 scheme developed by Khairoutdinov and Kogan (2000) (“KK scheme” hereafter) relates the
 77 autoconversion with N_c and q_c as follows:

$$\left(\frac{\partial q_r}{\partial t}\right)_{auto} = f_{auto}(q_c, N_c) = C q_c^{\beta_q} N_c^{\beta_N}, \quad (1)$$

78 where q_c and N_c have units of kg kg^{-1} and cm^{-3} , respectively; the parameter $C = 1350$, and the
 79 two exponents $\beta_q = 2.47$, $\beta_N = -1.79$ are obtained through a nonlinear regression between the
 80 variables q_c and N_c and the autoconversion rate derived from large-eddy simulation (LES) with
 81 bin-microphysics spectra.

82 Having a highly accurate microphysical parameterization — specifically, highly accurate
 83 local microphysical process rates — is not sufficient for an accurate simulation of warm-rain
 84 processes in GCMs. Clouds can have significant structures and variations at the spatial scale much
 85 smaller than the typical grid size of GCMs ($10 \sim 100 \text{ km}$) (*Barker et al., 1996; e.g., Cahalan and*
 86 *Joseph, 1989; Lebsock et al., 2013; Wood and Hartmann, 2006; Zhang et al., 2019*). Therefore,
 87 GCMs need to account for these subgrid-scale variations in order to correctly calculate grid-mean
 88 autoconversion and accretion rates. Pincus and Klein (2000) nicely illustrate this dilemma. Given
 89 subgrid-scale variability represented as a distribution $P(x)$ of some variable x , for example the q_c
 90 in Eq. (1), a grid-mean process rate is calculated as $\langle f(x) \rangle = \int f(x)P(x)dx$, where $f(x)$ is the
 91 formula for the local process rate. For nonlinear process rates such as autoconversion and accretion,
 92 the grid-mean process rates calculated from the subgrid-scale variability does not equal the process



rate calculated from the grid-mean value of x , i.e., $\langle f(x) \rangle \neq f(\langle x \rangle)$. Therefore, calculating autoconversion and accretion from grid-mean quantities introduces biases arising from subgrid-scale variability. To take this effect into account, a parameter E is often introduced as part of the parameterization such that $\langle f(x) \rangle = E \cdot f(\langle x \rangle)$. Following the convention of previous studies, E is referred to as the “enhancement factor” (EF) here. Given the autoconversion parameterization scheme, the magnitude of EF is primarily determined by cloud horizontal variability within a GCM grid. Unfortunately, because most GCMs do not resolve subgrid cloud variation, the value of EF is often simply assumed to be a constant for the lack of better options. The EF for KK autoconversion scheme due to subgrid q_c variation is assumed to be 3.2 in the two-moment scheme by Morrison and Gettelman (2008), which is employed in the widely used Community Atmosphere Model (CAM).

A number of studies have been carried out to better understand the horizontal variations of cloud microphysics in MBL cloud and the implications for warm rain simulations in GCMs. Most of these studies have been focused on the subgrid variation of q_c . Morrison and Gettelman (2008) and several later studies (Boutle *et al.*, 2014; Hill *et al.*, 2015; Lebsock *et al.*, 2013; Zhang *et al.*, 2019) showed that the subgrid variability q_c and thereby the EF are dependent on cloud regime and cloud fraction (f_c). They are generally smaller over the closed-cell stratocumulus regime with higher f_c and larger over the open-cell cumulus regime that often has a relatively small f_c . The subgrid variance of q_c is also dependent on the horizontal scale (L) of a GCM grid. Based on the combination of in situ and satellite observations, Boutle *et al.* (2014) found that the subgrid q_c variance first increases quickly with L when L is below about 20 km, then increases slowly and seems to approach to an asymptotic value for larger L . Similar spatial dependence is also reported in Huang *et al.* (2014), Huang and Liu (2014), Xie and Zhang (2015), and Wu *et al.* (2018) which



are based on the ground radar retrievals from the Department of Energy (DOE) Atmospheric Radiation Measurement (ARM) sites. The cloud-regime and horizontal-scale dependences have inspired a few studies to parameterize the subgrid q_c variance as a function of either f_c or L or a combination of the two (*e.g.*, Ahlgrimm and Forbes, 2016; Boutle *et al.*, 2014; Hill *et al.*, 2015; Xie and Zhang, 2015; Zhang *et al.*, 2019).

The aforementioned studies have an important limitation. They consider only the impacts of subgrid q_c variations on the EF but ignore the impacts of subgrid variation of N_c and its covariation with q_c . Based on cloud fields from large-eddy simulation, Larson and Griffin (2013) and later Kogan and Mechem (2014; 2016) elucidated that it is important to consider the covariation of q_c and N_c to derive a physically complete and accurate EF for the autoconversion parameterization. Lately, on the basis of MBL cloud observations from the Moderate Resolution Imaging Spectroradiometer (MODIS) Zhang *et al.* (2019) (hereafter referred to as Z19) elucidate that the subgrid variation of N_c tends to further increase the EF for the autoconversion process in addition to the EF due to q_c variation. The effect of q_c - N_c covariation on the other hand depends on the sign of the q_c - N_c correlation. A positive q_c - N_c correlation would lead to an EF <1 that partly offsets the effects of q_c and N_c variations. Although Z19 shed important new light on the EF problem for the warm rain process, their study also suffers from limitations due to the use of satellite remote sensing data. First, as a passive remote sensing technique, MODIS cloud product can only retrieve the column-integrated cloud optical thickness and the cloud droplet effective radius at cloud top, from which the column-integrated cloud liquid water path (LWP) is estimated. As a result of using LWP, instead vertically resolved observations the vertical dependence of the q_c and N_c horizontal variabilities are ignored in Z19. Second, the N_c retrieval from MODIS is based on several important assumptions, which can lead to large uncertainties (see review by



139 (*Grosvenor et al., 2018*). Furthermore, MODIS cloud retrieval product is known to suffer from
140 several inherent uncertainties, such as the three-dimensional radiative effects(*e.g., Zhang and*
141 *Platnick, 2011; Zhang et al., 2012; 2016*), which in turn can lead to large uncertainties in the
142 estimated EF.

143 This study is a follow up of Z19. To overcome the limitations of satellite observations, we
144 use the in situ measurements of MBL cloud from a recent DOE field campaign, the Aerosol and
145 Cloud Experiments in the Eastern North Atlantic (ACE-ENA), to investigate the subgrid variations
146 of q_c and N_c , as well as their covariation, and the implications for the simulation of autoconversion
147 simulation in GCMs. A main focus of this investigation is to understand the vertical dependence
148 of the q_c and N_c horizontal variations within the MBL clouds. This aspect has been neglected in
149 Z19 as well as most previous studies (*Boutle et al., 2014; Lebsock et al., 2013; Xie and Zhang,*
150 *n.d.*). A variety of microphysical processes, such as adiabatic growth, collision-coalescence,
151 entrainment mixing, can influence the vertical structure of MBL clouds. At the same time, these
152 processes also vary horizontally at the subgrid scale of GCMs. As a result, the horizontal variations
153 of q_c and N_c , as well as their covariation, and therefore the EFs may depend on the vertical location
154 inside the MBL clouds. It is important to understand this dependence for several reasons. First, the
155 warm rain process is usually initialized at cloud top where the autoconversion process of the cloud
156 droplets gives birth to embryo drizzle drops. The accretion process is, on the other hand, more
157 important in the lower part of the cloud (*Wood, 2005b*). Thus, a better understanding of the vertical
158 dependence of horizontal variations of q_c and N_c inside of MBL cloud could help us understand
159 how the EF should be modeled in the GCMs. Second, a good understanding of the vertical
160 dependence of q_c and N_c variation inside of MBL clouds will also help us understand the
161 limitations in the previous studies, such as Z19, that use the column-integrated products for the



162 study of EF. Finally, this investigation may also be useful for modeling other processes, such as
163 aerosol-cloud interactions, in the GCMs.

164 Therefore, our main objectives in this study are to: 1) better understand the horizontal
165 variations of q_c and N_c , as well as their covariation in MBL clouds, in particular their dependence
166 on the vertical height in cloud; 2) elucidate the implications for the EF of the autoconversion
167 parameterization in GCMs. The rest of the paper is organized as follows: we will describe the data
168 and observations used in this study in Section 2 and explain how we select the cases from the ACE-
169 ENA campaign for our study in Section 3. We will present cases studies in Section 4 and 5. Finally,
170 the results and findings from this study will be summarized and discussed in Section 6.

171

172 **2. Data and Observations**

173 The data and observations used for this study are from two main sources: the in-situ
174 measurements from the ACE-ENA campaign and the ground-based observations from the ARM
175 ENA site. The ENA region is characterized by persistent subtropical MBL clouds that are
176 influenced by different seasonal meteorological conditions and a variety of aerosol sources (*Wood*
177 *et al.*, 2015). A modeling study by Carslaw *et al.* (2013) found the ENA to be one of regions over
178 the globe with the largest uncertainty of aerosol indirect effect. As such, the ENA region attracted
179 substantial attention over the past few decades for aerosol-cloud interaction studies. From April
180 2009 to December 2010 the DOE ARM program deployed its ARM Mobile Facility (AMF) to the
181 Graciosa Island (39.09°N, 28.03°W) for a measurement field campaign targeting the properties of
182 cloud, aerosol and precipitation in the MBL (CAP-MBL) in the Azores region of ENA (*Wood et*
183 *al.*, 2015). The measurements from the CAP-MBL campaign have proved highly useful for a
184 variety of purposes, from understanding the seasonable variability of clouds and aerosols in the



185 MBL of the ENA region (*Dong et al., 2014; Rémillard et al., 2012*) to improving cloud
 186 parameterizations in the GCMs (*Zheng et al., 2016*) and to validating the space-borne remote
 187 sensing products of MBL clouds (*Zhang et al., 2017*). The success of the CAP-MBL revealed that
 188 the ENA has an ideal mix of conditions to study the interactions of aerosols and MBL clouds. In
 189 2013 a permanent measurement site is established by the ARM program on Graciosa Island as its
 190 newest permanent atmospheric observatories, also known as the ENA site (*Voyles and Mather,*
 191 *2013*).

192 **2.1. In situ measurements from the ACE-ENA campaign**

193 The Aerosol and Cloud Experiments in ENA (ACE-ENA) project was “*motivated by the*
 194 *need for comprehensive in situ characterizations of boundary-layer structure and associated*
 195 *vertical distributions and horizontal variabilities of low clouds and aerosol over the Azores*”
 196 (*Wang et al., 2016*). The ARM Aerial Facility (AAF) Gulfstream-1 (G-1) aircraft was deployed
 197 during two intensive measurement periods (IOPs), the summer 2017 IOP from June 21 to July 20,
 198 2017 and the winter 2018 IOP from January 15 to February 18, 2018. Over 30 research flights (RF)
 199 were carried out during the two IOPs around the ARM ENA site on Graciosa Island that sampled
 200 a large variety of cloud and aerosol properties along with the meteorological conditions.

201 Table 1 summarizes the in-situ measurements from the ACE-ENA campaign used in this
 202 study. The location and velocity of G1 aircraft, and the environment meteorological conditions
 203 during the flight (temperature, humidity, and wind velocity) are taken from Aircraft-Integrated
 204 Meteorological Measurement System 20-Hz (AIMMS-20) dataset (*Beswick et al., 2008*). The size
 205 distribution of cloud droplets, and the corresponding q_c and N_c are obtained from the fast cloud
 206 droplet probe (FCDP) measurement. The FCDP measures the concentration and size of cloud
 207 droplets in the diameter size range from 1.5 to 50 μm in 20 size bins with an overall uncertainty



of size around $3\text{ }\mu\text{m}$ (Lance *et al.*, 2010; SPEC, 2019). Following previous studies (Wood, 2005a), we adopt a $r^* = 20\text{ }\mu\text{m}$ as the threshold to separate cloud droplets from drizzle drops, i.e., drops with $r < r^*$ are considered as cloud droplets. After the separation, the q_c and N_c are derived from the FCDP droplet size distribution measurements. As an evaluation, we compared our FCDP-derived q_c results with the direct measurements of q_c from the multi-element water content system (WCM-2000) also flown during the ACE-ENA and found an excellent agreement. We also performed a couple of sensitivity tests in which we perturbed the value of r^* by $\pm 5\text{ }\mu\text{m}$. The perturbation shows little impact on the results shown in sections 4 and 5. The cloud droplet spectrum from the FCDP is available at a frequency of 10 Hz. Since the typical horizontal speed of the G-1 aircraft during the in-cloud leg is about 100 m s^{-1} , the spatial sampling rate these instruments is on the order of 10 m for the FCDP.

2.2. Ground observations from ARM ENA site

In addition to the in-situ measurements, ground measurements from the ARM ENA site are also used to provide ancillary data for our studies. In particular, we will use the Active Remote Sensing of Cloud Layers product (ARSCL; (Clothiaux *et al.*, 2000; Kollias *et al.*, 2005) which blends radar observations from the Ka-band ARM zenith cloud radar (KAZR), micropulse lidar (MPL), and the ceilometer to provide information on cloud boundaries and the mesoscale structure of cloud and precipitation. The ARSCL product is used to specify the vertical location of the G1 aircraft and thereby the in-situ measurements with respect to the cloud boundaries, i.e., cloud base and top (see example in Figure 1). In addition, the radar reflectivity observations from KAZR, alone with in situ measurements, are used to select the precipitating cases for our study. Note that the ARSCL product is from the vertically pointing instruments, which sometimes are not



collocated with the in-situ measurements from G1 aircraft. As explained later in the next section,
 only those cases with a reasonable collocation are selected for our study.

3. Case selections

3.1. ACE-ENA flight pattern

The section provides a brief overview of the G1 aircraft flight patterns during the ACE-
 ENA and explains the method for cases selections for our study using the July 18, 2017 RF as an
 example. As shown in Table 2, a variety of MBL conditions were sampled during the two IOPs of
 the ACE-ENA campaign, from mostly clear-sky to thin stratus and drizzling stratocumulus. In this
 study, we are interested in the RFs that encountered the drizzling stratocumulus clouds, since our
 objective is to understand the implications of subgrid cloud variation for the autoconversion
 process. The basic flight patterns of G1 aircraft in the ACE-ENA included spirals to obtain vertical
 profiles of aerosol and clouds, and legs at multiple altitudes, including below cloud, inside cloud,
 at the cloud top, and in the free troposphere. As an example, Figure 1a shows the horizontal
 location of the G1 aircraft during the July 18, 2017 RF which is the “golden case” for our study as
 explained in the next section. The corresponding vertical track of the aircraft is shown in Figure
 1b overlaid on the reflectivity curtain of ground based KAZR. In this RF, the G1 aircraft repeated
 multiple times of horizontal level runs in a “V” shape at different vertical levels inside, above and
 below the MBL (see Figure 1b). The lower tip of the “V” shape is located at the ENA site on
 Graciosa island. The average wind in the upper MBL (i.e., 900 mb) is approximately Northwest.
 So, the left side of the V-shape horizontal level runs is along the wind and the right side cross the
 wind. Note that the horizontal velocity of the G1 aircraft is approximately 100 m s⁻¹. Since the
 duration of these selected “V” shape hlegs is between 580 s and 700 s, their total horizontal length
 is roughly 60 km, with each side of the “V” shape ~30 km. These “V” shape horizontal level runs,



with one side along and the other cross the wind, are a common sampling strategy used in the ACE-ENA to observe the properties of aerosol and cloud at different vertical levels of the MBL. In our study we use the vertical location of the G1 aircraft from the AIMMS to identify continuous horizontal flight tracks which are referred to as the “hleg”. For the July 18, 2017 case, a total of 13 hlegs are identified as shown in Figure 1b. Among them, the hleg 5, 6, 7, 8, 10, 11, and 12 are the seven V-shape horizontal level runs inside the MBL cloud. Together they provide an excellent set of samples of the MBL cloud properties at different vertical levels of a GCM grid box of about 30 km. As aforementioned, Boutle et al. (2014) found that the horizontal variance of q_c increases with the horizontal scale L slowly when L is larger than about 20 km. Therefore, although the horizontal sampling of the selected hlegs is only about 30 km, the lessons learned here could yield useful insights for larger GCM grid sizes. In addition to the hlegs, we also identified the vertical penetration legs in each flight, referred to as the “vlegs”, from which we will obtain the vertical structure of the MBL, along with the properties of cloud and aerosol.

3.2. Case selection

As illustrated in Figure 1 a and b for the July 18, 2017 RF, the criteria we used to select the RF cases and the hlegs within the RF can be summarized as follows:

- The RF encounters precipitating MBL clouds according to both pilot report and radar reflectivity observations from the ground-based KAZR.
- The RF samples multiple continuous in-cloud hlegs at different vertical levels with the horizontal length of at least 10 km and cloud fraction larger than 10% (i.e., the fraction of a hleg with $q_c > 0.01 \text{ g m}^{-3}$ must exceed 10% of the total length of that hleg)
- Moreover, the selected hlegs must sample the same region repeatedly in terms of horizontal track but different vertical levels in terms of vertical track. Take the July 18, 2017 case as



an example. The hleg 5, 6, 7, 8 follow the same “V” shape horizontal track (see Figure 1a) but sample different vertical levels of the MBL clouds (see Figure 1b). Such hlegs provide us the horizontal sampling needed to study the subgrid horizontal variations of the cloud properties and, at the same time, the chance to study the vertical dependence of the horizontal cloud variations.

- Finally, the RF needs to have at least one vleg and the cloud boundary derived from the vleg is largely consistent with that derived from the ground-based measurements. This requirement is to ensure that the vertical locations of the selected hlegs with respect to cloud boundaries can be specified. For example, as shown in Figure 1b according to the ground-based observations, the hlegs 5 and 10 of July 18, 2017 case are close to cloud base, while hlegs 8 and 12 close to cloud top (see also Figure 4).

The above requirements together pose a strong constraint on the observation. Fortunately, thanks to the careful planning of the RF which had already taken studies like ours into consideration, we are able to select a total of four RF cases as summarized in Table 3. We will first focus on the “golden case—July 18, 2017 RF and then investigate if the lessons learned from the July 18, 2017 RF also apply to the other three cases.

4. A study of the July 18, 2017 case

4.1. Horizontal and vertical variations of cloud microphysics

On July 18, 2017, the North Atlantic is controlled by the Icelandic low to the north and the Azores high to the south (see Figure 2b), which is a common pattern of large-scale circulation during the summer season in this region (*Wood et al., 2015*). The Azores is at the southern tip of the cold air sector of a frontal system where the fair-weather low-level stratocumulus clouds are dominant (see satellite image in Figure 2a). The RF on this day started around 8:30 UTC and ended



around 12 UTC. As explained in the previous section, we selected 7 hlegs from this RF that horizontally sampled the same region repeatedly in a similar “V” shaped track but vertically at different levels. The radar reflectivity observation from the ground based KAZR during the same period peaks around 10 dBZ indicating the presence of significant drizzle inside the MBL clouds.

Among the 7 selected hlegs, the hlegs 5, 6, 7 and 8 are 4 consecutive “V” shape tracks, with hlegs 5 close to cloud base and hleg 8 close to cloud top. The hlegs 10,11 and 12 are another set of consecutive “V” shape tracks with hlegs 10 and 12 close to cloud base and top, respectively (see Figure 1). Using $q_c > 0.01 \text{ gm}^{-3}$ as a threshold for cloud, the cloud fraction (f_c) of all these hlegs is close to unity (i.e., overcast), except for the two hlegs close to cloud base ($f_c=46\%$ for hleg 5 and $f_c=51\%$ for hleg 10). The q_c and N_c derived from the in situ FCDP measurements for these selected hleg are plotted in Figure 3 as a function of UTC time. It is evident from Figure 3 that both q_c and N_c have significant horizontal variations. At cloud base (see Figure 3d for hleg 5 and Figure 3g for hleg 10) the q_c varies from 0.01 gm^{-3} (i.e., the lower threshold) up to about 0.4 gm^{-3} and the N_c from 25 cm^{-3} up to 150 cm^{-3} , with the mean values around 0.08 gm^{-3} and 65 cm^{-3} , respectively. Such strong variations of cloud microphysics could be contributed by a number of factors. One can see from the ground radar and lidar observations in Figure 1b that the height of cloud base varies significantly. As a result, the horizontal legs may not really sample the cloud base. In addition, the variability in updraft at cloud base cloud lead to the variability in the activation and growth of cloud condensation nuclei (CCN). In the middle of the MBL cloud, i.e., hleg 6 (Figure 3c), 7 (Figure 3b) and 11 (Figure 3f), the mean value of q_c is significantly larger than that of cloud base hlegs while the variability is reduced. The mean value of q_c keeps increasing toward cloud top to $\sim 0.73 \text{ gm}^{-3}$ in hleg 8 (Figure 3a) and to $\sim 0.53 \text{ gm}^{-3}$ in hleg 12



(Figure 3e), respectively. In contrast, the horizontal variability of q_c seems to increase in comparison with those observed in mid-level hlegs.

To obtain a further understanding of the vertical variations of cloud microphysics, we analyzed the cloud microphysics observations from the two green-shaded vlegs 1 and 3 in Figure 1b. The vertical profile of the mean q_c and N_c from these two vlegs are shown in Figure 4a and Figure 4b, respectively, with over-plotted the mean and standard deviation of the q_c and N_c derived from the 7 selected hlegs. Overall, the vertical profiles of the q_c and N_c are qualitatively aligned with the classic adiabatic MBL cloud structure (Brenguier *et al.*, 2000; Martin *et al.*, 1994). That is, the N_c remains relatively a constant (see Figure 4b) while the q_c increases approximately linearly with height from cloud base upward as a result of condensation growth (see Figure 4a), except for the very top of the cloud, i.e., the entrainment zone where the dry air entrained from the above mixes with the humid cloudy air in the MBL. In previous studies, a so-called inverse relative variance, ν , is often used to quantify the subgrid variations of cloud microphysics. It is defined as follows

$$\nu_X = \frac{\langle X \rangle^2}{\sigma_X^2}, \quad (2)$$

where X is either q_c (i.e., $\nu_X = \nu_{q_c}$) or N_c (i.e., $\nu_X = \nu_{N_c}$). $\langle X \rangle$ and σ_X are the mean value and standard deviation of X , respectively. As such the smaller the ν value the larger the horizontal variation of X in comparison with the mean value. As shown in Figure 4c, the ν_{q_c} and ν_{N_c} derived from the selected hlegs follow a similar vertical pattern: they both increase first from cloud base upward and then decrease in the entrainment zone, with the turning point somewhere around 1 km (i.e., around hleg 7 and 11). It indicates that both q_c and N_c have significant horizontal variabilities at cloud base which may be a combined result of horizontal fluctuations of dynamics (e.g., updraft) and thermodynamics (e.g., temperature and dynamics), as well as horizontal variations of aerosols.



343 The horizontal variabilities of both q_c and N_c both decrease upward toward cloud top until the
 344 entrainment zone where both variabilities increase again.

345 So far, in all the analyses above the variations of q_c and N_c have been considered
 346 separately and independently. As pointed out in several previous studies, the co-variation of q_c
 347 and N_c could have an important impact on the EF for the autoconversion process in GCMs (*Kogan*
 348 *and Mechem, 2016; Larson and Griffin, 2013; Zhang et al., 2019*). This point will be further
 349 elucidated in detail in the next section. Figure 5 shows the joint distributions of q_c and N_c for the
 350 7 selected hlegs and the corresponding linear correlation coefficients as a function of height are
 351 shown in Figure 4d. For the sake of reference, the linear correlation coefficient between $\ln(q_c)$
 352 and $\ln(N_c)$, i.e., the ρ_L that will be introduced later in Eq. (4), is also plotted in Figure 4d.
 353 Looking first at the hlegs 10, 11 and 12, i.e., the 2nd group of consecutive “V” shape legs, there is
 354 a clear increasing trend of the correlation between q_c and N_c from cloud bottom ($\rho = 0.75$ for
 355 hleg 10) to cloud top ($\rho = 0.95$ for hleg 12). The picture based on the hlegs 5, 6, 7, and 8 is more
 356 complex. As shown in Figure 5, the joint distributions of q_c and N_c of hleg 6 (Figure 5b), hleg 7
 357 (Figure 5c) and, to a less extent, hleg 8 (Figure 5d) all exhibit a clear bimodality. Further analysis
 358 reveals that each of the two modes in these bimodal distributions approximately corresponds to
 359 one side of the “V” shape track. As aforementioned, for all the selected 7 “V” shape hlegs, the left
 360 side is along the wind and the right side across the wind (see Figure 1). To illustrate this difference,
 361 the across-wind side of the hleg is shaded in yellow in Figure 3. It is intriguing to note that the N_c
 362 from the across-wind side of the hleg are systematically larger than those from the along-wind side,
 363 while their q_c values are largely similar. As a result of this bimodality of N_c , the correlation
 364 coefficients between q_c and N_c is significantly smaller for the hlegs 6 ($\rho = 0.22$) and 7 ($\rho = 0.31$)
 365 in comparison with other hlegs. However, if the two sides of the “V” shape tracks are considered



separately, then the q_c and N_c become more correlated, except for the cross-wind side of hleg 6 which still exhibits to some degree a bimodal joint distributions of q_c and N_c . In spite of the bimodality, there is evidently a general increasing trend of the correlation between q_c and N_c from cloud base toward cloud top. At the cloud top, the q_c and N_c correlation coefficient can be as high as $\rho = 0.95$ for hleg 12 (see Figure 5e). As explain in the next section, this close correlation between q_c and N_c has important implications for the simulation of autoconversion enhancement factor.

As a summary, the above phenomenological analysis of the July 18, 2017 RF reveals the following features of the horizontal and vertical variations of cloud microphysics. Vertically, the mean values of q_c and N_c qualitatively follow the adiabatic structure of MBL cloud, i.e., q_c increases linear with height and N_c remains largely invariant above cloud base. Even though the joint distribution of q_c and N_c exhibits a bimodality in several hlegs, their correlation generally increases with height and can be as high as $\rho = 0.95$ at cloud top. Horizontally, both q_c and N_c have a significant variability at cloud base, which tends to first decrease upward and then increase in the uppermost part of cloud close to the entrainment zone.

4.2. Implications for the EF for the autoconversion rate parameterization

As explained in the introduction, in GCMs the autoconversion process is usually parameterized as a highly nonlinear function of q_c and N_c , e.g., the KK scheme in Eq. (1). In such parameterization, an EF is needed to account for the bias caused by the nonlinearity effect. A variety of methods have been proposed and used in the previous studies to estimate the EF (*Larson and Griffin, 2013; Lebsock et al., 2013; Pincus and Klein, 2000; Zhang et al., 2019*). The methods used in this study are based on Z19. Only the most relevant aspects are recapped here. Readers are referred to Z19 for detail.



389 If the subgrid variations of q_c and N_c , as well as their covariation, are known, then the EF
 390 can be estimated based on its definition as follows

$$E = \frac{\int_0^\infty \int_0^\infty q_c^{\beta_q} N_c^{\beta_N} P(q_c, N_c) dq_c dN_c}{\langle q_c \rangle^{\beta_q} \langle N_c \rangle^{\beta_N}}, \quad (3)$$

391 where $\langle q_c \rangle$ and $\langle N_c \rangle$ are the grid-mean value, $P(q_c, N_c)$ is the joint probability density function
 392 (PDF) of q_c and N_c . Some previous studies approximate the $P(q_c, N_c)$ as a bivariate lognormal
 393 distribution as follows:

$$P(q_c, N_c) = \frac{1}{2\pi q_c N_c \sigma_{q_c} \sigma_{N_c} \sqrt{1 - \rho_L^2}} \exp\left(-\frac{\zeta}{2}\right) \quad (4)$$

$$\zeta = \frac{1}{1 - \rho_L^2} \left[\left(\frac{\ln q_c - \mu_{q_c}}{\sigma_{q_c}} \right)^2 - 2\rho \left(\frac{\ln q_c - \mu_{q_c}}{\sigma_{q_c}} \right) \left(\frac{\ln N_c - \mu_{N_c}}{\sigma_{N_c}} \right) + \left(\frac{\ln N_c - \mu_{N_c}}{\sigma_{N_c}} \right)^2 \right],$$

394 where μ_X and σ_X are, respectively, the mean and standard deviation of $\ln(X)$, where X is either
 395 q_c or N_c . ρ_L is the linear correlation coefficient between $\ln(q_c)$ and $\ln(N_c)$, (Larson and Griffin,
 396 2013; Lebsock et al., 2013; Zhang et al., 2019). It should be noted here that ρ_L is fundamentally
 397 different from ρ (i.e., the linear correlation coefficient between q_c and N_c). On the other hand, we
 398 found that for all the selected hlegs ρ and ρ_L are in an excellent agreement (see Figure 4d). In fact,
 399 ρ and ρ_L can be used interchangeably in the context of this study without any impact on the
 400 conclusions. Nevertheless, interested readers may find more detailed discussion of the relationship
 401 between ρ and ρ_L in Larson and Griffin (2013).

402 Substituting $P(q_c, N_c)$ in Eq. (4) into Eq. (3) yields a formula for EF that consists of the
 403 following three terms

$$E = E_q(\nu_{q_c}, \beta_q) \cdot E_N(\nu_{N_c}, \beta_N) \cdot E_{COV}(\rho_L, \beta_q, \beta_N, \nu_{q_c}, \nu_{N_c}), \quad (5)$$



where $E_q(v_{q_c}, \beta_q)$ corresponds to the enhancing effect of the subgrid variation of q_c , if q_c follows a marginal lognormal distribution, i.e., $P(x) = \frac{1}{\sqrt{2\pi}x\sigma} \exp\left(-\frac{(\ln x - \mu)^2}{2\sigma^2}\right)$. It is a function of the inverse relative variance v_q in Eq. (2) as follows:

$$E_q(v_{q_c}, \beta_q) = \left(1 + \frac{1}{v_{q_c}}\right)^{\frac{\beta_q^2 - \beta_q}{2}}. \quad (6)$$

Similarly, the $E_N(v_{N_c}, \beta_N)$ below corresponds to the enhancing effect of the subgrid variation of N_c , if N_c follows a marginal lognormal distribution,

$$E_N(v_{N_c}, \beta_N) = \left(1 + \frac{1}{v_{N_c}}\right)^{\frac{\beta_N^2 - \beta_N}{2}}. \quad (7)$$

The third term $E_{COV}(\rho_L, \beta_q, \beta_N, v_{q_c}, v_{N_c})$ in Eq. (5)

$$E_{COV}(\rho_L, \beta_q, \beta_N, v_{q_c}, v_{N_c}) = \exp(\rho_L \beta_q \beta_N \sigma_{q_c} \sigma_{N_c}), \quad (8)$$

corresponds to the impact of the co-variation of q_c and N_c on the EF. Because $\beta_q > 0$ and $\beta_N < 0$, if q_c and N_c are negatively correlated (i.e., $\rho_L < 0$) then the $E_{COV} > 1$ and acts as an enhancing effect on the autoconversion rate computation. In contrast, if q_c and N_c are positively correlated (i.e., $\rho_L > 0$), then the $E_{COV} < 1$ which becomes a suppressing effect on the autoconversion rate computation.

As aforementioned, most previous studies of the EF consider only the impact of subgrid q_c variation (i.e., only the E_q term). The impacts of subgrid N_c variation as well as its covariation with q_c have been largely overlooked in observational studies, in which, the E_q is often derived from the observed subgrid variation of q_c based on the definition of EF, i.e.,



$$E_q = \frac{\int_0^\infty q_c^{\beta_q} P(q_c) dq_c}{\langle q_c \rangle^{\beta_q}}, \quad (9)$$

where $P(q_c)$ is the observed subgrid PDF of q_c . Alternatively, E_q have also been estimated from the inverse relative variance v_q by assuming the subgrid variation of q_c to follow either the lognormal distribution, in which case E_q is given in Eq. (6).

Similar to E_N , if only the effect of subgrid N_c is considered, the corresponding E_N can be derived from the following two ways, one from the observed subgrid PDF $P(N_c)$ based on the definition of EF, i.e.,

$$E_N = \frac{\int_0^\infty N_c^{\beta_N} P(N_c) dN_c}{\langle N_c \rangle^{\beta_N}}, \quad (10)$$

and the other based on Eq. (7) from the relative variance v_{N_c} by assuming the subgrid N_c variation to follow the lognormal distribution.

Now, we put the in-situ q_c and N_c observations from the selected hlegs in the theoretical framework of EF described above and investigate the following questions:

1) What is the (“observation-based”) EF derived based on Eq. (3) from the observed joint PDF $P(q_c, N_c)$?

2) How well does the (“bi-logarithmic”) EF derived based on Eq. (5) by assuming that the covariation of q_c and N_c follows a bi-variate lognormal agree with the observation-based EF?

3) What is the relative importance of the E_q , E_N , and E_{COV} terms in Eq. (5) in determining the value of EF?

4) What is the error of considering only E_q and omitting the E_N and E_{COV} terms?

5) How do the observation-based EFs from Eq. (3) and the E_q , E_N , E_{COV} terms vary with vertical height in cloud?



These questions are addressed in the rest of this section. Focusing first on the E_q in Figure 6a, the E_q derived from observation based on Eq. (9) (solid circle) shows a clear decreasing trend with height between cloud base at around 700 m to about 1 km, with value reduced from about 3 to about 1.2. Then, the value of E_q increases slightly in the cloud top hlegs 8 and 12. The E_q derived based on Eq. (6) by assuming lognormal distribution (open circle) has a very similar vertical pattern, although the value is slightly overestimated in comparison with the observation-based result. The vertical pattern of E_q can be readily explained by how the subgrid variation of q_c in Figure 4c. The E_N derived from observation (solid triangle) in Figure 6b shows a similar vertical pattern as E_q , i.e., first decreasing with height from cloud base to about 1.2 km and then increasing with height in the uppermost part of cloud. The E_N derived based on Eq. (7) by assuming a lognormal distribution (open triangle) show a large error compared with the observation-based values, especially at cloud base (i.e., hleg 5 and 10) and cloud top (i.e., hleg 8 and 12).

Using hleg10 as an example, we further investigated the cause for the error in lognormal-based EFs in comparison with those diagnosed from the observation. As shown in Figure 7a the observed q_c is slightly negatively skewed in logarithmic space by the small values. Because the autoconversion rate is proportional to $q_c^{2.47}$, the negatively skewed q_c also leads to a negatively skewed E_q in Figure 7b. As a result, the leg-averaged E_q diagnosed from the observation is slightly smaller than that derived based on Eq. (6) by assuming a lognormal distribution. The negative skewness also explains the large error in E_N for hleg 10 seen on Figure 6b. As shown in Figure 7c the observed N_c is also negatively skewed, to a much larger extent in comparison with q_c . Because the autoconversion rate is proportional to $N_c^{-1.79}$, the highly negatively skewed N_c results in a



highly *positively* skewed E_N in Figure 7d. As a result, the E_N diagnosed from the observation is much larger than that derived based on Eq. (7) by assuming a lognormal distribution.

The E_q and E_N reflect only the individual contributions of subgrid q_c and N_c variations to the EF. The effect of the covariation of q_c and N_c , i.e., the E_{COV} is shown in Figure 6c. Interestingly, the value of E_{COV} is smaller than unity for all the selected hlegs. As explained in Eq. (8), $E_{COV} < 1$ is a result of a positive correlation between q_c and N_c , as seen in Figure 4d. Therefore, in these hlegs the covariation of the q_c and N_c has *suppressing* effect on the EF, in contrast to the enhancing effect of E_q and E_N . This result is qualitatively consistent with Z19 who found that the vertically integrated liquid water path (LWP) of MBL clouds is in general positively correlated with the N_c estimated from the MODIS cloud retrieval product and, as a result, $E_{COV} < 1$ over most of the tropical oceans. Because of the relationship in Eq. (8), the value E_{COV} is evidently negatively proportional to the correlation coefficient ρ_L in Figure 4d. The largest value is seen in hleg 6 and 7 in which the bimodal joint distribution of q_c and N_c results in a small ρ_L . The smallest $E_{COV} = 0.21$ is seen in hleg 12, as result of a strong correlation between q_c and N_c ($\rho_L = 0.96$) and moderate σ_q and σ_N .

Finally, the EF that accounts for all factors, including the individual variations of q_c and N_c , as well as their covariation, is shown in Figure 6d. Focusing first on the observation-based results (solid star), i.e., E in Eq. (3), evidently there is a decreasing trend from cloud base (e.g., $E = 2.2$ for hleg 5 and $E = 1.59$ for hleg 10) to cloud top (e.g., $E = 1.20$ for hleg 8 and $E = 1.02$ for hleg 12). The E derived based on Eq. (5) by assuming the bi-variate lognormal distribution between q_c and N_c (i.e., open star in Figure 6d) are generally larger than the observation-based results, in particularly for hleg 6 and 7. To investigate the reason for this error, we compared the observed joint PDF between q_c and N_c for hleg 7 with the diagnosed bi-variate lognormal



distribution in Figure 8. As already noted, the observed q_c and N_c follow a bimodal distribution which leads to a rather small correlation coefficient ρ_L . The bi-variate lognormal distribution interprets this small ρ_L as an abroad unimodal distribution (dashed contour line), which leads to an overestimate of EF.

Finally, it is intriguing to note that the value of $E = E_q \cdot E_N \cdot E_{COV}$ in Figure 6d is comparable to E_q Figure 6a, which indicates that the enhancing effect of $E_N > 1$ in Figure 6b is partially canceled by the suppressing effect of $E_{COV} < 1$ in Figure 6c. As aforementioned, many previous studies of the EF consider only the effect of E_q but overlook the effect of E_N and E_{COV} . The error in the studies would be quite large if it were not for a fortunate error cancellation.

5. Other Selected Cases

In addition to the July 18, 2017 RF, we also found another 3 RFs that meet our criterions as described in Section 3 for case selection. As summarized in Table 3 and shown in Figure 1c-h, the July 20, 2017 and Jan. 19, 2018 RFs sampled the MBL clouds around the ENA site repeatedly in a “V” shape horizontal pattern similar to the July 18, 2017 RF. In contrast, the Feb. 11, 2018 RF is different from the other three cases in two aspects. First, its horizontal sampling pattern is a simple straight line. Second, the boundary layer is significantly deeper, with a mean cloud top height around 1.5 km in comparison to the ~ 1 km cloud top height in other RFs. Due to limited space, we cannot present the detailed case studies of these RFs. Instead, we view them collectively and investigate whether the lessons learned from the July 18, 2017 RF, especially those about the EF in Section 4.2, also apply to the other cases.

In order to compare the hlegs from different RFs, we first normalize the altitude of each hleg with respect to the minimum and maximum values of all selected hlegs in each RF as follows:



$$z_{hleg}^* = \frac{z_{hleg} - z_{min}}{z_{max} - z_{min}}, \quad (11)$$

where z_{hleg}^* is the normalized altitude for each hleg in a RF, z_{min} and z_{max} are the altitude of the lowest and highest hleg in the corresponding RF. Defined this way, z_{hleg}^* is bounded between 0 and 1. Alternatively, z_{hleg}^* could also be defined with respect to the averaged cloud top (z_{top}) and base (z_{base}) as inferred from the KAZR or vlegs. However, because of the variation of cloud top and cloud base heights, as well as the collocation error, the z_{hleg}^* would often become significantly larger than 1 or smaller than 0, if z_{hleg}^* were defined with respect to z_{top} and z_{base} , making results confusing and difficult to interpret.

Figure 9 shows the observation based EFs for all the selected hlegs from the 4 selected RFs as a function of the z_{hleg}^* . As shown in Figure 9a, the E derived based on (3) that accounts for the covariation of q_c and N_c has a decreasing trend from cloud base to cloud top. This is consistent with the result from the July 18, 2017 case in Figure 6d. However, neither the E_q in Figure 9b nor the E_N in Figure 9c shows a clear dependence on z_{hleg}^* in comparison with the results of July 18th, 2017 case in Figure 6a and b. Note that the E_q and E_N are influenced by a number of factors, such as horizontal distance and cloud fraction, in addition to vertical height. It is possible that the differences in other factors outweigh the vertical dependence here. Interestingly, the linear correlation coefficient ρ between q_c and N_c in Figure 9d shows an increasing trend with z_{hleg}^* that is statistically significant (R-value= 0.50 and P-value=0.02), despite a few outliers including the aforementioned hleg 6 and 7 from July 18, 2017 case and also the hleg 16 from Jan. 19, 2018 case. It turns out that the joint distribution of q_c and N_c in the hleg 16 of the Jan. 19, 2018 is also bimodal (similar to Figure 5b and not shown here), leading to a small ρ_L . Nevertheless, the increasing trend of ρ with z_{hleg}^* in Figure 9d is consistent with what we found in the July 18, 2017 case (see Figure



4d). As evident from Eq. (8), an increase of ρ_L would lead to a decrease of E_{COV} . Since neither E_q nor E_N shows a clear dependence on z_{hleg}^* , the decrease of E_{COV} with z_{hleg}^* seems to play an important role in the determining the value of E . Another line of evidence supporting this role is the fact that both E_q and E_N are quite large for the cloud top hlegs, while in contrast the values of corresponding E that accounts for the covariation of q_c and N_c are much smaller. For example, the E_q for two hlegs from the Feb. 11, 2018 RF exceeds 8 but the corresponding E values are smaller than 1.2 which is evidently a result of large ρ_L and thereby small E_{COV} .

As aforementioned, many previous studies of the EF for the autoconversion rate parameterization consider only the effect of subgrid q_c variation but ignore the effects of subgrid N_c variation, and its covariation with q_c . To understand the potential error, we compared the E_q and E both derived based on observations in Figure 10. Apparently, E_q is significantly larger than E_q for most of the selected hlegs, which implies that the considering only subgrid q_c variation would likely lead to an overestimation of EF. This is an interesting result. Note that $E_N \geq 1$ by definition and therefore $E_q > E$ is possible only when the covariation of q_c and N_c has a *suppressing* effect, instead of enhancing. Once again, this result demonstrates the importance of understanding the covariation of q_c and N_c for understanding the EF for autoconversion rate parameterization.

Having looked at the observation-based EFs, we now check if the EFs derived based on assumed PDFs (e.g., lognormal or bi-variate lognormal distributions) agree with the observation-based results. As shown in Figure 11a, the E_q based on Eq. (6) that assumes a lognormal distribution for the subgrid variation of q_c is in an excellent agreement with the observation-based results. In contrast, the comparison is much worse for the E_N in Figure 11b, which is not surprising given the results from the July 18, 2017 case in Figure 6b. As one can see from Figure 5, the



550 marginal PDF of N_c is often broad and sometimes even bimodal. The deviation of the observed
551 N_c PDF from the lognormal distribution is probably the reason for the large difference of E_N in
552 Figure 11b. As shown in Figure 11c, the E derived based on Eq. (5) by assuming a bi-variate
553 lognormal function for the joint distribution of q_c and N_c tends to be larger than the observation-
554 based results. The reason for this overestimation is because the joint PDF of q_c and N_c is often
555 bimodal as seen in Figure 5. In such case, the small correlation coefficient ρ due to the bimodality
556 is misinterpreted as a rather broad bi-variate lognormal distribution which in turn leads to an
557 overestimated E value.

558 6. Summary and Discussion

559 In this study we derived the horizontal variations of q_c and N_c , as well as their covariations
560 in MBL clouds based on the in-situ measurements from the recent ACE-ENA campaign and
561 investigated the implications for the EF of the autoconversion parameterization in the GCMs. The
562 main findings can be summarized as follows:

- 563 • In the July 18, 2017 case, the vertical variation of the mean values of q_c and N_c roughly
564 follows the adiabatic structure. The horizontal variances of q_c and N_c first decrease from
565 cloud base upward toward the middle of the cloud and then increase in the entrainment
566 zone. The correlation between of q_c and N_c generally increases from cloud base to cloud
567 top.
- 568 • In other selected cases, the horizontal variances of q_c and N_c show no statistically
569 significant dependence on the vertical height in cloud. However, the increasing trend of
570 the correlation between q_c and N_c from cloud base to cloud top remains robust.



- 571 • In a few selected “V” shape hlegs, the q_c and N_c follow a bimodal joint distribution
- 572 which leads to a poor linear correlation between them. The two modes in the bimodal
- 573 distribution correspond to the along-wind and cross-wind sides of the “V” shape hlegs.
- 574 • The observation-based physically complete E that accounts for the covariation of q_c and
- 575 N_c has a robust decreasing trend from cloud base to cloud top, which can be explained
- 576 by the increasing trend of the q_c and N_c correlation from cloud base to cloud top.
- 577 • The E estimated by assuming a monomodal bi-variate lognormal joint distribution
- 578 between q_c and N_c systematically overestimates the observation-based results,
- 579 especially for the hlegs with a bimodal q_c and N_c joint distribution. The omission of the
- 580 N_c variation and its covariation with q_c tends to lead to an overestimation of EF despite
- 581 the error cancellation.

582 These results provide the following two new understandings of the EF for the autoconversion
 583 parameterization that have potentially important implications for GCM. First, our study indicates
 584 that the physically complete E has a robust decreasing trend from cloud base to cloud top. Because
 585 the autoconversion process is most important at the cloud top, this vertical dependence of EF
 586 should be taken into consideration in the GCM parametrization scheme. Second, our study
 587 indicates that effect of the q_c and N_c correlation plays a critical role in determining the EF. Lately
 588 a few novel modeling techniques have been developed to provide the coarse resolution GCMs
 589 information of subgrid cloud variation, such as the PDF-based higher-order turbulence closure
 590 method—Cloud Layer Unified By Binormals, CLUBB (Golaz *et al.*, 2002; Guo *et al.*, 2015;
 591 Larson *et al.*, 2002). These models are able to provide parameterized subgrid variance of q_c which
 592 can be used in turn to estimate E_q . However, as shown in our study the E_q tends to overestimate
 593 the EF.



594 Our study has a couple of important limitations. First of all, our results are based on a
595 handful cases from a single field campaign. The lessons learned here need to be further examined
596 based on more data or tested in modeling studies. Second, we study provides only a
597 phenomenological analysis of the horizontal variations cloud microphysics in the MBL clouds and
598 the implications for the EF. Ongoing modeling research based on a comprehensive LES model is
599 being conducted to identify and elucidate the process-level physical mechanisms behind our
600 observational results. Finally, this study is focused on the KK parameterization in estimating the
601 enhancement factors resulting from subgrid variability of q_c , N_c and q_c - N_c covariance. The
602 specific values are expected to differ when applied to other autoconversion parameterizations with
603 different power-law exponents.
604



605 **Acknowledgement:**

606 Z. Zhang acknowledges the financial support from the Atmospheric System Research (Grant DE-
607 SC0020057) funded by the Office of Biological and Environmental Research in the US DOE Office of
608 Science. The computations in this study were performed at the UMBC High Performance Computing
609 Facility (HPCF). The facility is supported by the U.S. National Science Foundation through the MRI
610 program (Grants CNS-0821258 and CNS-1228778) and the SCREMS program (Grant DMS-0821311),
611 with substantial support from UMBC. Co-author D. Mechem was supported by subcontract OFED0010-
612 01 from the University of Maryland Baltimore County and the U.S. Department of Energy's Atmospheric
613 Systems Research grant DE-SC0016522.

614

615



616

617

618 *Table 1 In situ cloud instruments from ACE-ENA campaign used in this study*

Instruments	Measurements	Frequency	Resolution	Accuracy
AIMMS	P, T, RH, u,v,w	20 Hz	/	/
F-CDP	DSD 2~50 μm	10 Hz	1 -2 μm	2 μm
2DS	DSD 10 ~2500 μm	1 Hz	25 – 150 μm	10 μm

619

620

621 *Table 2 conditions of MBL sampled during the two IOPs of ACE-ENA campaign*

Conditions Sampled	Research Flights	
	IOP1: June-July 2017	IOP2: Jan.-Feb. 2018
Mostly clear	6/23, 6/29, 7/7	2/16
Thin Stratus	6/21, 6/25, 6/26, 6/28, 6/30, 7/4, 7/13	1/28, 2/1, 2/10, 2/12
Solid StCu	7/6, 7/8, 7/15	1/30
Multi-layer StCu	7/11, 7/12	1/24, 1/29, 2/8
Drizzling StCu/Cu	7/3, 7/17, 7/18, 7/19, 7/20	1/19, 1/21, 1/25, 1/26, 2/9, 2/11, 2/15, 2/18, 2/19

622

623 *Table 3 A summary of selected RFs, and the selected hlegs and vlegs within each RF.*

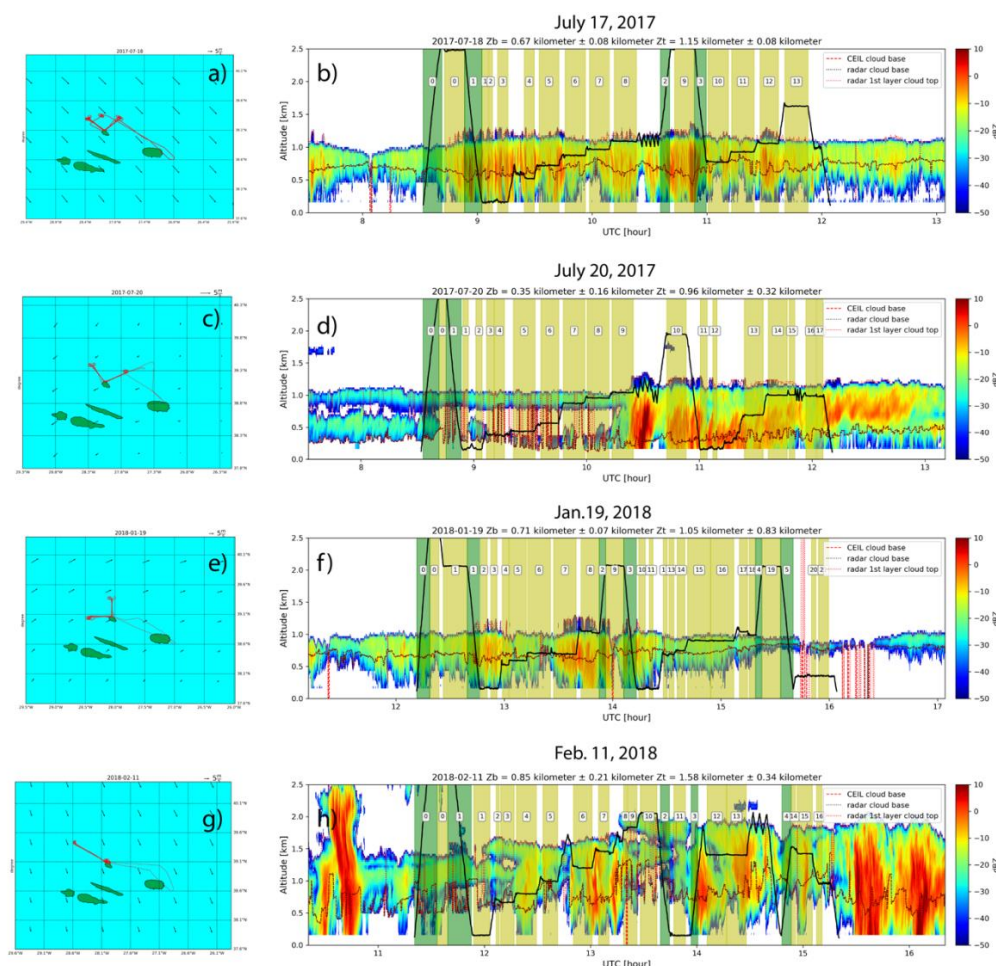
Research Flight	Sampling pattern	Selected hlegs	Selected vlegs
July 18, 2017 IOP1	“V” shape	5, 6, 7, 8, 10, 11, 12	0, 1, 3
July 20, 2017 IOP1	“V” shape	5, 6, 7, 8, 9, 13, 14	0, 1
Jan. 19, 2018 IOP2	“V” shape	6, 7, 8, 15, 16	0, 1, 3
Feb. 11, 2018 IOP2	Straight-line	4, 5, 6, 7, 12, 13	0, 1

624

625



626



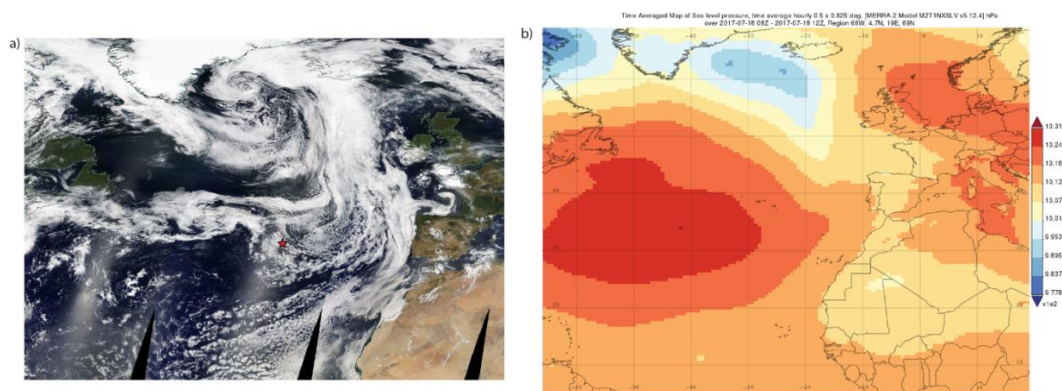
627

628 Figure 1 Four selected RF from the ACE-ENA for this study. (a) horizontal flight track of the G1
 629 aircraft (red) during the July 18, 2017 RF. Small arrows in the figure indicate the wind vector at
 630 900 mb. (b) vertical flight track of G1(thick black line) overlaid on the radar reflectivity contour
 631 by the ground-based KZAR. The dotted lines in the figure indicate the cloud base and top retrievals
 632 from ground-based radar and CEIL instruments. (c) and (d) same as (a) and (b), except for July
 633 20, 2017 RF. (e) and (f) are for Jan. 19, 2018 RF. (g) and (h) are for Feb. 11, 2018 RF.

634



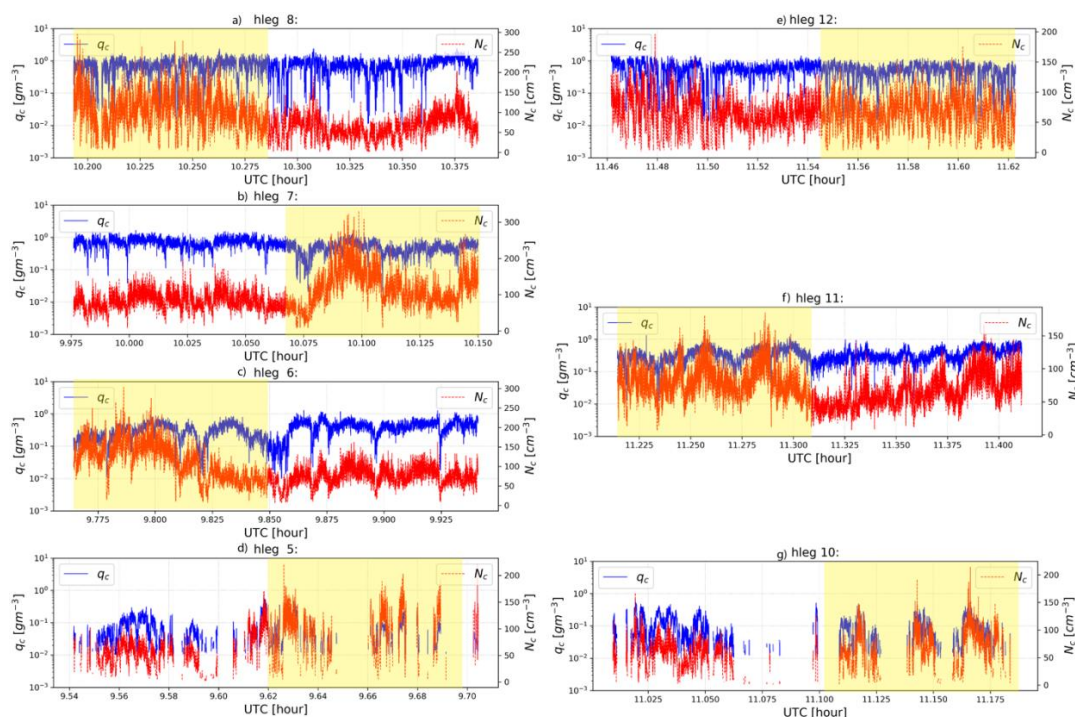
635



636

637 Figure 2 **(a)** The real color satellite image of the ENA region on July 18, 2017 from the MODIS.
 638 The small red star marks the location of the ARM ENA site on the Graciosa Island; **(b)** The
 639 averaged sea level pressure (SLP) of the ENA region on July 18, 2017 from the Merra-2
 640 reanalysis.

641



642

643 Figure 3 The horizontal variations of q_c (red) and N_c (blue) for each selected hleg derived from
 644 the in situ FCDP instrument. The yellow-shaded time period in each plot corresponds to the
 645 cross-wind side of the “V” shape flight track and the unshaded part corresponds to the along-
 646 wind part. Note that plots are ordered such that the (a) hleg 8 and (e) hleg 12 are close to cloud
 647 top; (b) hleg 6, (c) hleg 7 and (f) hleg 11 are sampled in the middle of clouds; (d) hleg 5 and (g)
 648 hleg 10 are close to cloud base

649

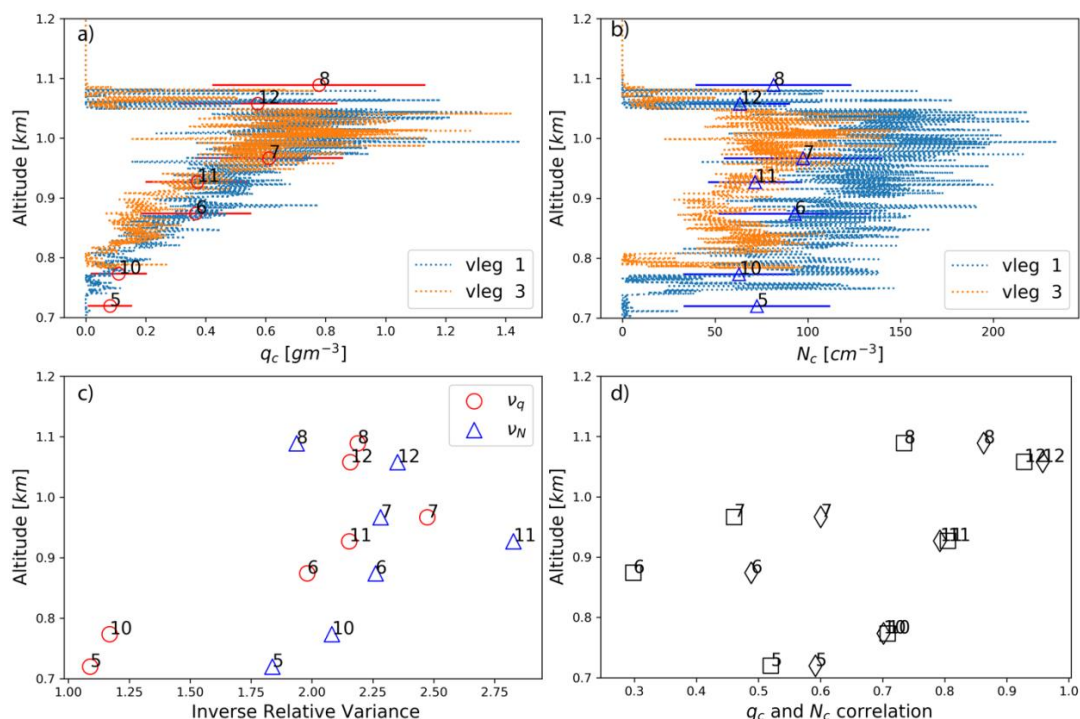
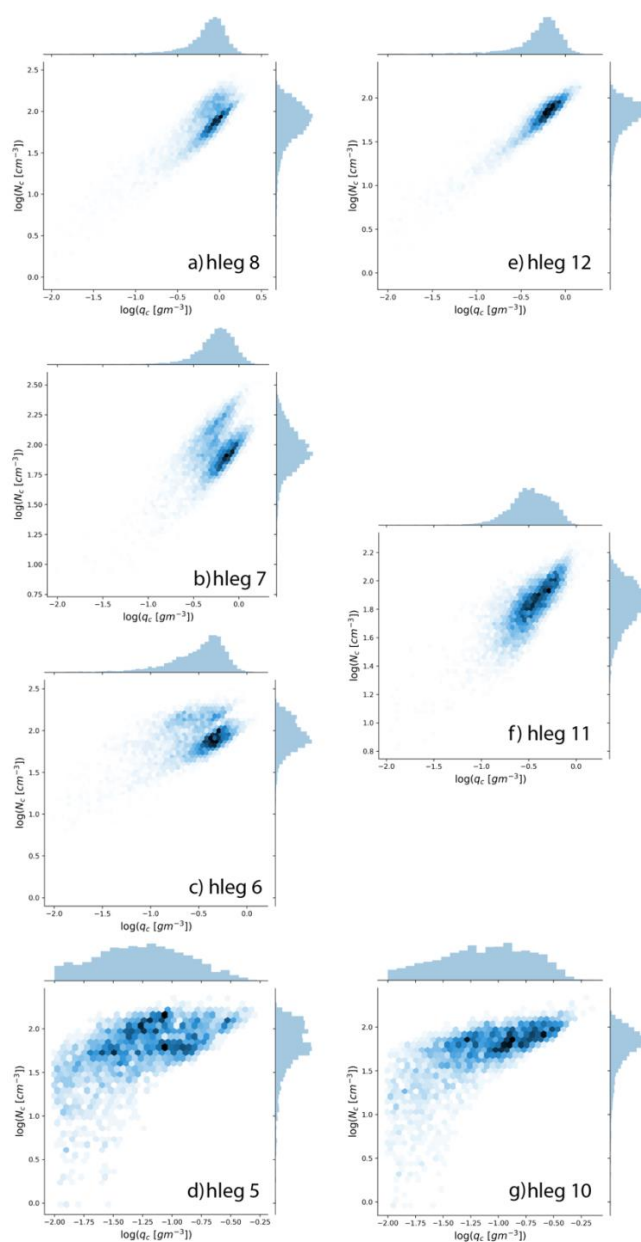


Figure 4 (a) The vertical profiles of q_c derived from the vlegs (dotted lines) of the July 18, 2017 case. The overplotted red errorbars indicate the mean values and standard deviations of the q_c derived from the selected hlegs at different vertical levels. (b) same as (a) except for N_c . (c) The vertical profile of the inverse relative variances (i.e., mean divided by standard deviation) of N_c (red circle) and N_c (blue triangle) derived from the hleg; (d) The vertical profile of the linear correlation coefficient between $\ln(q_c)$ and $\ln(N_c)$, i.e., ρ_L (square) and linear correlation coefficient between q_c and N_c , i.e., ρ (diamond).



661

662 Figure 5 The joint distributions of the q_c and N_c , along with the marginal histograms, for the 7
 663 selected hleg from the July 18, 2017 RF. Same as Figure 3, the plots are ordered such that the (a)
 664 hleg 8 and (e) hleg 12 are close to cloud top; (b) hleg 6, (c) hleg 7 and (f) hleg 11 are sampled in
 665 the middle of clouds; (d) hleg 5 and (g) hleg 10 are close to cloud base.

666

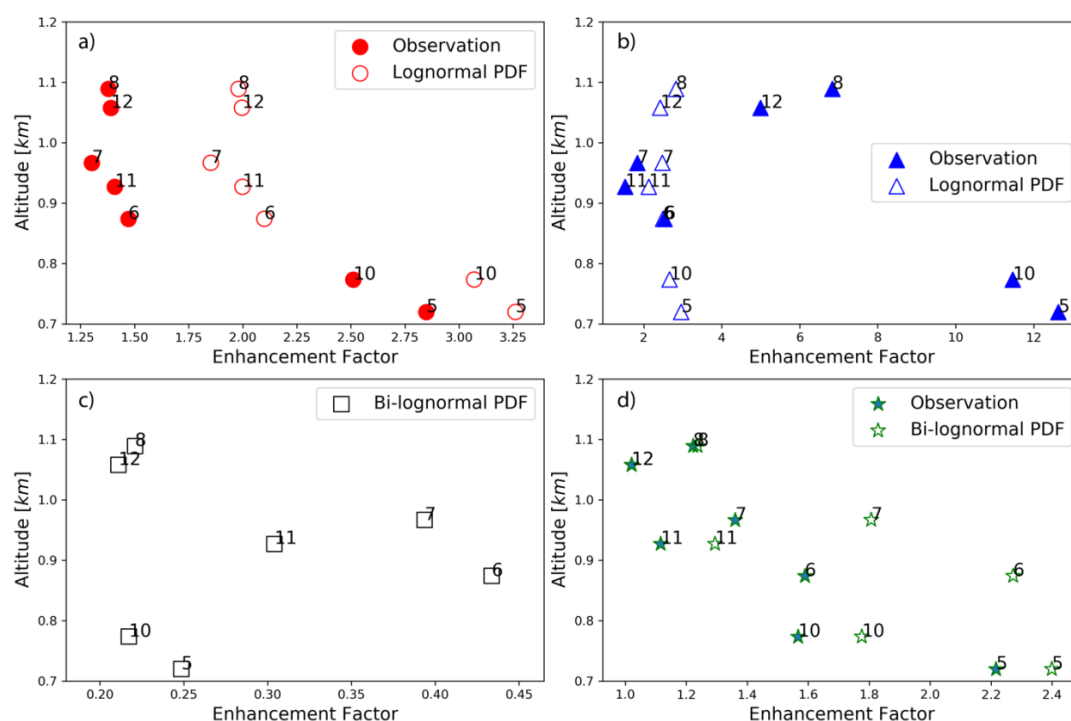
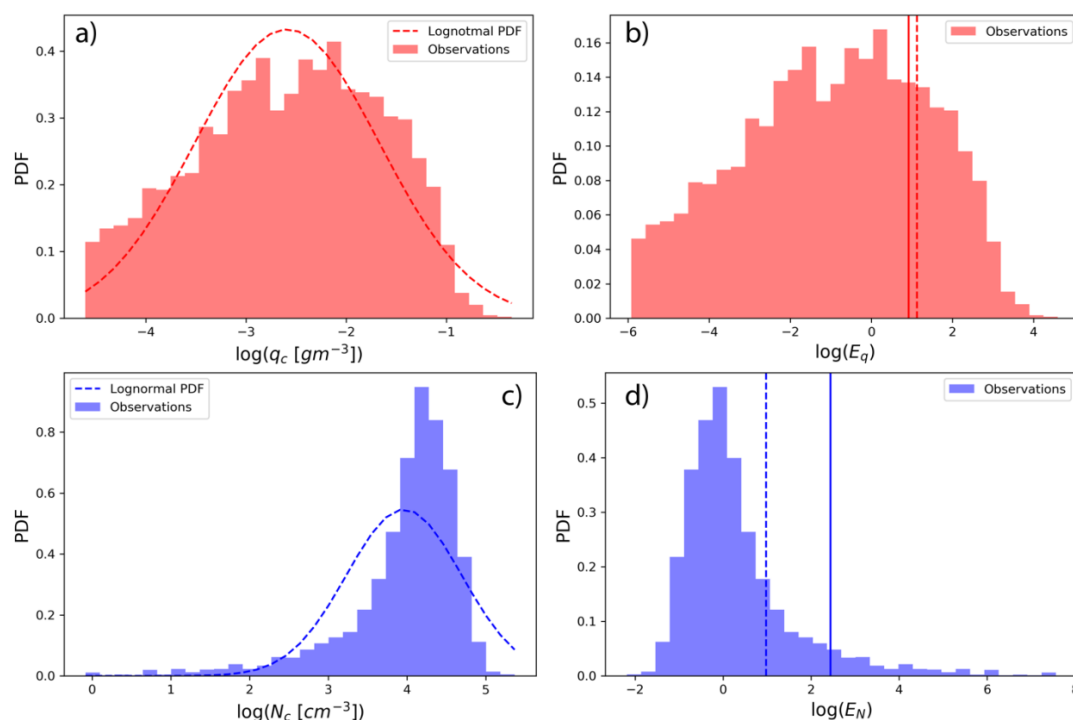


Figure 6 (a) E_q as a function of height derived from observation based on Eq. (9) (solid circle) and from the inverse relative variance v_q assuming lognormal distribution based on Eq. (6) (open circle). (b) E_N as a function of height derived from observation based on Eq. (10) (solid triangle) and from the inverse relative variance v_N assuming lognormal distribution based on Eq. (7) (open triangle). (c) E_{COV} derived based on Eq. (8) as a function of height. (d) E as a function of height derived from observation based on Eq. (3) (solid star) and based on Eq. (5) assuming a bi-lognormal distribution (open star). The numbers beside the symbols in the figure correspond to the numbers of the 7 selected hlegs.



679



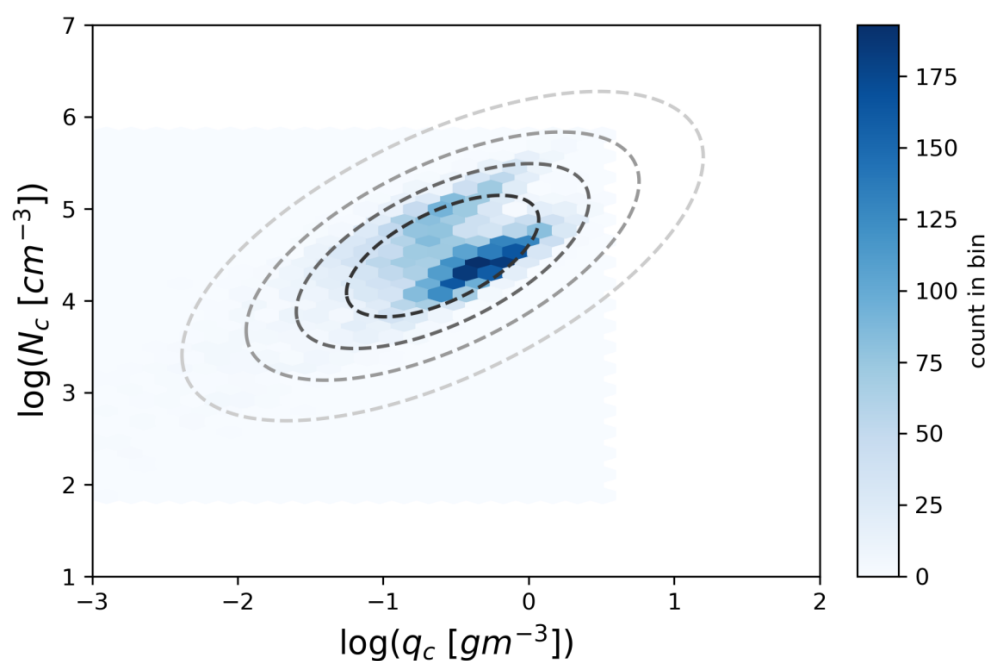
680

681 Figure 7 **(a)** Histogram of $\ln(q_c)$ based on observations from the hleg 10 (bars) and the lognormal
 682 PDF (dashed line) based on the μ_{q_c} and σ_{q_c} of hleg 10. **(b)** The histogram of $\ln(E_q)$ diagnosed
 683 from the observed q_c based on Eq. (9). The two vertical lines correspond to the leg-averaged
 684 $\ln(E_q)$ derived based on the observed q_c (solid) and the lognormal PDF (dashed line),
 685 respectively. **(c)** Histogram of $\ln(N_c)$ based on observations from the hleg 10 (bars) and the
 686 lognormal PDF (dashed line) based on the μ_{N_c} and σ_{N_c} of hleg 10. **(d)** The histogram of $\ln(E_N)$
 687 diagnosed from the observed q_c based on Eq. (10). The two vertical lines correspond to the leg-
 688 averaged $\ln(E_N)$ derived based on the observed N_c (solid) and the lognormal PDF (dashed line),
 689 respectively.

690



691



692

693 Figure 8 The joint PDF between $\ln(q_c)$ and $\ln(N_c)$ based on observations from hleg 7 (color
 694 contour) in comparison with the bi-variate lognormal PDF (dashed line contour) which is derived
 695 based on the μ_{q_c} , σ_{q_c} , μ_{N_c} , σ_{N_c} , and ρ_L of hleg 7.

696

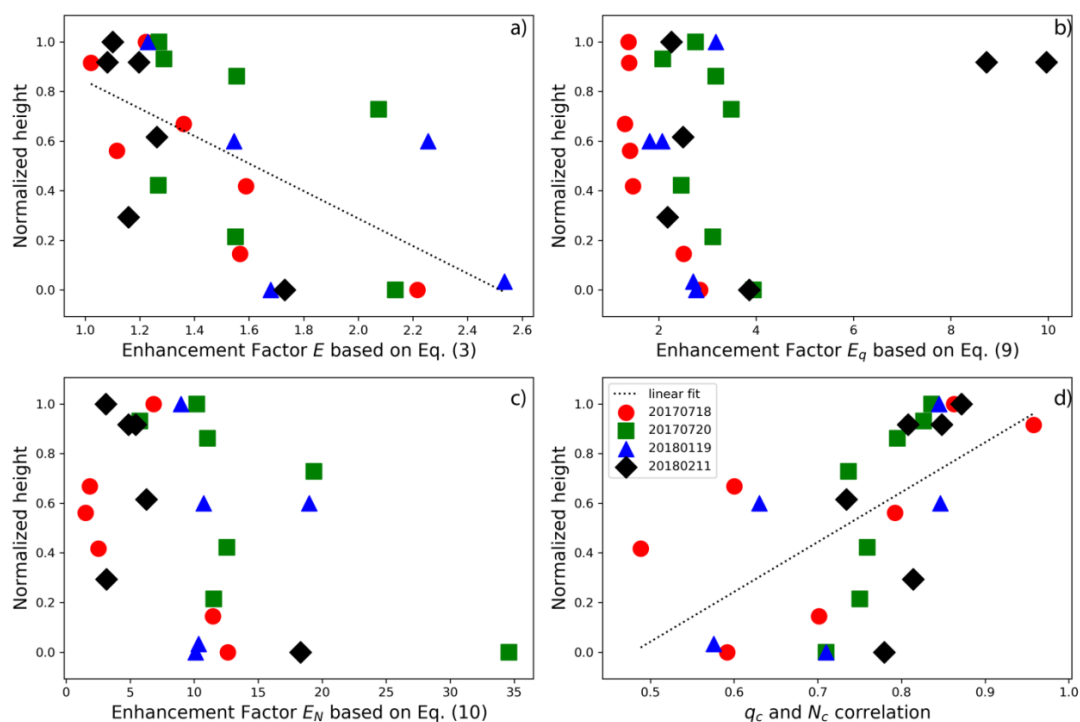
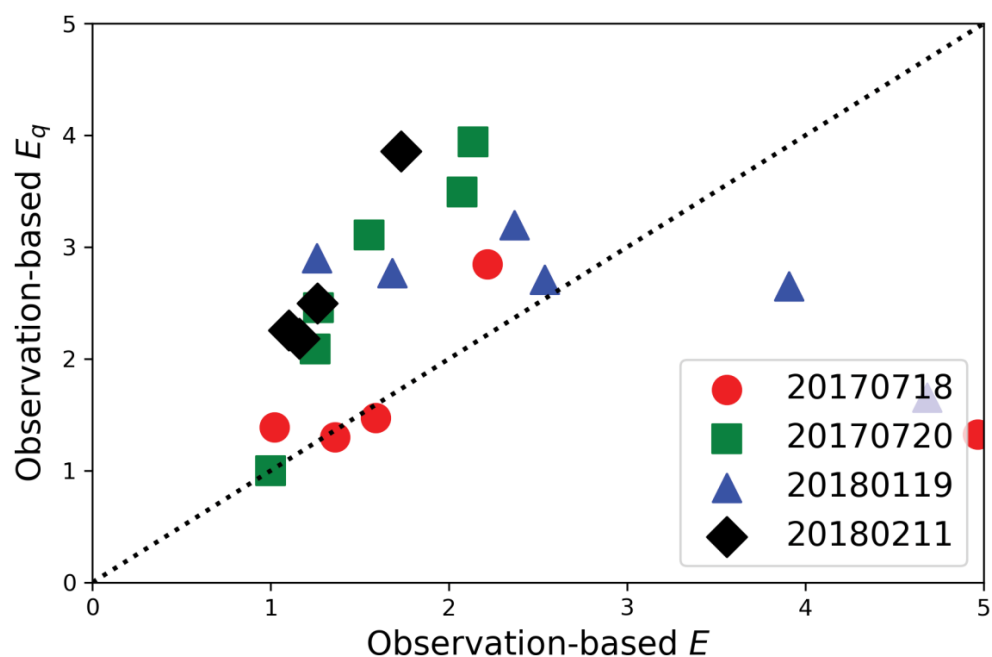


Figure 9 (a) The observation-based E derived from Eq. (3) that accounts for the covariation of q_c and N_c . (b) The observation-based E_q derived from Eq. (9) that accounts for only the subgrid variation of q_c . (c) The observation-based E_N derived from Eq. (10) that accounts for only the subgrid variation of N_c . (d) The correlation coefficient between q_c and N_c . All quantities are plotted as a function of the normalized height z_{hleg}^* in Eq. (11). The dashed lines correspond to a linear fit of the data when the fitting is statistically significant (i.e., P-value < 0.05).



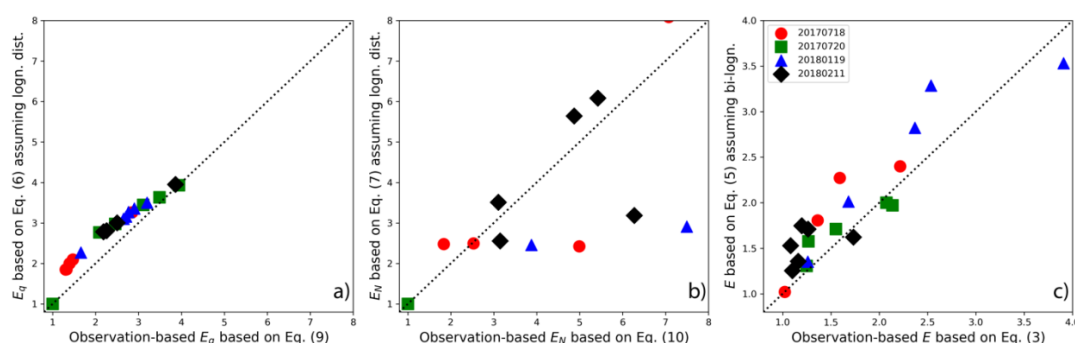
709

710 Figure 10 A comparison of observation-based E and observation-based E_q for all the selected
 711 hlegs from all 4 selected RF.

712



713



714

715 Figure 11 **(a)** A comparison of observation-based E_q derived based on Eq. (9) and E_q derived
 716 based on Eq. (6) assuming lognormal distribution for subgrid q_c observations for all the selected
 717 hlegs. **(b)** A comparison of observation-based E_N derived based on Eq. (10) and E_N derived
 718 based on Eq. (7) assuming lognormal distribution or all the selected hlegs. **(c)** A comparison of
 719 observation-based E derived based on Eq. (3) and E derived based on Eq. (5) assuming bi-
 720 variate lognormal distribution for the subgrid joint distribution of q_c and N_c .

721

722



723

724 References:

- 725 Ahlgrim, M. and Forbes, R. M.: Regime dependence of cloud condensate variability observed
 726 at the Atmospheric Radiation Measurement Sites, *Quarterly Journal of the Royal Meteorological*
 727 *Society*, 142(697), 1605–1617, doi:10.1002/qj.2783, 2016.
- 728 Barker, H. W., Wielicki, B. A. and Parker, L.: A Parameterization for Computing Grid-
 729 Averaged Solar Fluxes for Inhomogeneous Marine Boundary Layer Clouds. Part II: Validation
 730 Using Satellite Data, [http://dx.doi.org/10.1175/1520-](http://dx.doi.org/10.1175/1520-0469(1996)053<2304:APFCGA>2.0.CO;2)
 731 [0469\(1996\)053<2304:APFCGA>2.0.CO;2](http://dx.doi.org/10.1175/1520-0469(1996)053<2304:APFCGA>2.0.CO;2), 53(16), 2304–2316 [online] Available from:
 732 [http://journals.ametsoc.org/doi/pdf/10.1175/1520-](http://journals.ametsoc.org/doi/pdf/10.1175/1520-0469%281996%29053%3C2304%3AAPFCGA%3E2.0.CO%3B2, 1996)
 733 [0469%281996%29053%3C2304%3AAPFCGA%3E2.0.CO%3B2](http://journals.ametsoc.org/doi/pdf/10.1175/1520-0469%281996%29053%3C2304%3AAPFCGA%3E2.0.CO%3B2, 1996), 1996.
- 734 Beswick, K. M., Gallagher, M. W., Webb, A. R., Norton, E. G. and Perry, F.: Application of the
 735 AvenTech AIMMS20AQ airborne probe for turbulence measurements during the Convective
 736 Storm Initiation Project, *Atmospheric Chemistry and Physics*, 8(17), 5449–5463,
 737 doi:10.5194/acp-8-5449-2008, 2008.
- 738 Bony, S. and Dufresne, J.-L.: Marine boundary layer clouds at the heart of tropical cloud
 739 feedback uncertainties in climate models, *Geophysical Research Letters*, 32(20), L20806,
 740 doi:10.1029/2005GL023851, 2005.
- 741 Bony, S., Stevens, B., Frierson, D. M. W., Jakob, C., Kageyama, M., Pincus, R., Shepherd, T. G.,
 742 Sherwood, S. C., Siebesma, A. P., Sobel, A. H., Watanabe, M. and Webb, M. J.: Clouds,
 743 circulation and climate sensitivity, *Nature Geoscience*, 8(4), 261–268, doi:10.1038/ngeo2398,
 744 2015.
- 745 Boucher, O., Randall, D., Artaxo, P., Bretherton, C., Feingold, G., Forster, P., Kerminen, V.-M.,
 746 Kondo, Y., Liao, H. and Lohmann, U.: Clouds and aerosols, in *Climate change 2013: The*
 747 *physical science basis. Contribution of working group I to the fifth assessment report of the*
 748 *intergovernmental panel on climate change*, pp. 571–657, Cambridge University Press. 2013.
- 749 Boutle, I. A., Abel, S. J., Hill, P. G. and Morcrette, C. J.: Spatial variability of liquid cloud and
 750 rain: observations and microphysical effects, *Quarterly Journal of the Royal Meteorological*
 751 *Society*, 140(679), 583–594, doi:10.1002/qj.2140, 2014.
- 752 Brenguier, J., Pawlowska, H. and Schüller, L.: Radiative properties of boundary layer clouds:
 753 Droplet effective radius versus number, 2000.
- 754 Cahalan, R. F. and Joseph, J. H.: Fractal statistics of cloud fields, *Monthly Weather Review*,
 755 117(2), 261–272, 1989.
- 756 Carslaw, K. S., Lee, L. A., Reddington, C. L., Pringle, K. J., Rap, A., Forster, P. M., Mann, G.
 757 W., Spracklen, D. V., Woodhouse, M. T., Regayre, L. A. and Pierce, J. R.: Large contribution of
 758 natural aerosols to uncertainty in indirect forcing, *Nature*, 503(7474), 67–71,
 759 doi:10.1038/nature12674, 2013.



- 760 Clothiaux, E. E., Marchand, R. T., Martner, B. E., Ackerman, T. P., Mace, G. G., Moran, K. P.,
 761 Miller, M. A. and Martner, B. E.: Objective Determination of Cloud Heights and Radar
 762 Reflectivities Using a Combination of Active Remote Sensors at the ARM CART Sites,
 763 [http://dx.doi.org/10.1175/1520-0450\(2000\)039<0645:ODOCHA>2.0.CO;2](http://dx.doi.org/10.1175/1520-0450(2000)039<0645:ODOCHA>2.0.CO;2), 39(5), 645–665,
 764 doi:10.1175/1520-0450(2000)039<0645:ODOCHA>2.0.CO;2, 2000.
- 765 Dong, X., Xi, B., Kennedy, A., Minnis, P. and Wood, R.: A 19-Month Record of Marine Aerosol–
 766 Cloud–Radiation Properties Derived from DOE ARM Mobile Facility Deployment at the Azores.
 767 Part I: Cloud Fraction and Single-Layered MBL Cloud Properties,
 768 <http://dx.doi.org/10.1175/JCLI-D-13-00553.1>, 27(10), 3665–3682, doi:10.1175/JCLI-D-13-
 769 00553.1, 2014.
- 770 Golaz, J.-C., Larson, V. E. and Cotton, W. R.: A PDF-Based Model for Boundary Layer Clouds.
 771 Part I: Method and Model Description, *JAS*, 59(24), 3540–3551, doi:10.1175/1520-
 772 0469(2002)059<3540:APBMFB>2.0.CO;2, 2002.
- 773 Grosvenor, D. P., Sourdeval, O., Zuidema, P., Ackerman, A., Alexandrov, M. D., Bennartz, R.,
 774 Boers, R., Cairns, B., Chiu, J. C., Christensen, M., Deneke, H., Diamond, M., Feingold, G.,
 775 Fridlind, A., Hunerbein, A., Knist, C., Kollias, P., Marshak, A., McCoy, D., Merk, D., Painemal,
 776 D., Rausch, J., Rosenfeld, D., Russchenberg, H., Seifert, P., Sinclair, K., Stier, P., van
 777 Diedenhoven, B., Wendisch, M., Werner, F., Wood, R., Zhang, Z. and Quaas, J.: Remote Sensing
 778 of Droplet Number Concentration in Warm Clouds: A Review of the Current State of Knowledge
 779 and Perspectives, *Reviews of Geophysics*, 56(2), 409–453, doi:10.1029/2017RG000593, 2018.
- 780 Guo, H., Golaz, J. C., Donner, L. J., Wyman, B., Zhao, M. and Ginoux, P.: CLUBB as a unified
 781 cloud parameterization: Opportunities and challenges, *Geophysical Research Letters*, 42(11),
 782 4540–4547, doi:10.1002/2015GL063672, 2015.
- 783 Hill, P. G., Morcrette, C. J. and Boutle, I. A.: A regime-dependent parametrization of subgrid-
 784 scale cloud water content variability, *Quarterly Journal of the Royal Meteorological Society*,
 785 141(691), 1975–1986, doi:10.1002/qj.2506, 2015.
- 786 Huang, D. and Liu, Y.: Statistical characteristics of cloud variability. Part 2: Implication for
 787 parameterizations of microphysical and radiative transfer processes in climate models, *Journal*
 788 *of Geophysical Research-Atmospheres*, 119(18), 10,829–10,843, doi:10.1002/2014JD022003,
 789 2014.
- 790 Huang, D., Campos, E. and Liu, Y.: Statistical characteristics of cloud variability. Part 1:
 791 Retrieved cloud liquid water path at three ARM sites, *Journal of Geophysical Research-*
 792 *Atmospheres*, 119(18), 10,813–10,828, doi:10.1002/2014JD022001, 2014.
- 793 Khairoutdinov, M. and Kogan, Y.: A New Cloud Physics Parameterization in a Large-Eddy
 794 Simulation Model of Marine Stratocumulus, *Mon. Wea. Rev.*, 128(1), 229–243 [online] Available
 795 from: [http://journals.ametsoc.org/doi/abs/10.1175/1520-](http://journals.ametsoc.org/doi/abs/10.1175/1520-0493(2000)128%3C0229%3AANCPPI%3E2.0.CO%3B2)
 796 [0493\(2000\)128%3C0229%3AANCPPI%3E2.0.CO%3B2](http://journals.ametsoc.org/doi/abs/10.1175/1520-0493(2000)128%3C0229%3AANCPPI%3E2.0.CO%3B2), 2000.
- 797 Kogan, Y. L. and Mechem, D. B.: A PDF-Based Microphysics Parameterization for Shallow
 798 Cumulus Clouds, *J. Atmos. Sci.*, 71(3), 1070–1089, doi:10.1175/JAS-D-13-0193.1, 2014.



- 799 Kogan, Y. L. and Mechem, D. B.: A PDF-Based Formulation of Microphysical Variability in
 800 Cumulus Congestus Clouds, *J. Atmos. Sci.*, 73(1), 167–184, doi:10.1175/JAS-D-15-0129.1,
 801 2016.
- 802 Kollias, P., ALBRECHT, B. A., Clothiaux, E. E., Miller, M. A., Johnson, K. L. and Moran, K. P.:
 803 The Atmospheric Radiation Measurement Program Cloud Profiling Radars: An Evaluation of
 804 Signal Processing and Sampling Strategies, <http://dx.doi.org/10.1175/JTECH1749.1>, 22(7),
 805 930–948, doi:10.1175/JTECH1749.1, 2005.
- 806 Lance, S., Brock, C. A., Rogers, D. and Gordon, J. A.: Water droplet calibration of the Cloud
 807 Droplet Probe (CDP) and in-flight performance in liquid, ice and mixed-phase clouds during
 808 ARCPAC, *AMT*, 3(6), 1683–1706, doi:10.5194/amt-3-1683-2010, 2010.
- 809 Larson, V. E. and Griffin, B. M.: Analytic upscaling of a local microphysics scheme. Part I:
 810 Derivation, *Quarterly Journal of the Royal Meteorological Society*, 139(670), 46–57,
 811 doi:10.1002/qj.1967, 2013.
- 812 Larson, V. E., Golaz, J.-C. and Cotton, W. R.: Small-Scale and Mesoscale Variability in Cloudy
 813 Boundary Layers: Joint Probability Density Functions, *J. Atmos. Sci.*, 59(24), 3519–3539,
 814 doi:10.1175/1520-0469(2002)059<3519:SSAMVI>2.0.CO;2, 2002.
- 815 Lebsock, M., Morrison, H. and Gettelman, A.: Microphysical implications of cloud-precipitation
 816 covariance derived from satellite remote sensing, *Journal of Geophysical Research-*
 817 *Atmospheres*, 118(12), 6521–6533, doi:10.1002/jgrd.50347, 2013.
- 818 Liu, Y. and Daum, P. H.: Parameterization of the Autoconversion Process. Part I: Analytical
 819 Formulation of the Kessler-Type Parameterizations, [http://dx.doi.org/10.1175/1520-](http://dx.doi.org/10.1175/1520-0469(2004)061<1539:POTAPI>2.0.CO;2)
 820 [0469\(2004\)061<1539:POTAPI>2.0.CO;2](http://dx.doi.org/10.1175/1520-0469(2004)061<1539:POTAPI>2.0.CO;2), 61(13), 1539–1548, doi:10.1175/1520-
 821 [0469\(2004\)061<1539:POTAPI>2.0.CO;2](http://dx.doi.org/10.1175/1520-0469(2004)061<1539:POTAPI>2.0.CO;2), 2004.
- 822 Lohmann, U. and Feichter, J.: Global indirect aerosol effects: a review, *ACP*, 5(3), 715–737,
 823 2005.
- 824 Martin, G., Johnson, D. and Spice, A.: The Measurement and Parameterization of Effective
 825 Radius of Droplets in Warm Stratocumulus Clouds., 51(13), 1823–1842, 1994.
- 826 Morrison, H. and Gettelman, A.: A New Two-Moment Bulk Stratiform Cloud Microphysics
 827 Scheme in the Community Atmosphere Model, Version 3 (CAM3). Part I: Description and
 828 Numerical Tests, *Journal of Climate*, 21(15), 3642–3659, doi:10.1175/2008JCLI2105.1, 2008.
- 829 Pincus, R. and Klein, S. A.: Unresolved spatial variability and microphysical process rates in
 830 large-scale models, *J. Geophys. Res.*, 105(D22), 27059–27065, doi:10.1029/2000JD900504,
 831 2000.
- 832 Rémillard, J., Kollias, P., Luke, E. and Wood, R.: Marine Boundary Layer Cloud Observations
 833 in the Azores, *Journal of Climate*, 25(21), 7381–7398, doi:10.1175/JCLI-D-11-00610.1, 2012.
- 834 SPEC: SPEC FCDP Technical Manual (Rev.2.0). 2019.



- 835 Voyles, J. W. and Mather, J. H.: *The Arm Climate Research Facility: A Review of Structure and*
 836 *Capabilities*, American Meteorological Society. 2013.
- 837 Wang, J., Dong, X. and Wood, R.: *Aerosol and Cloud Experiments in Eastern North Atlantic*
 838 *(ACE-ENA) Science Plan*, DOE Office of Science Atmospheric Radiation Measurement (ARM)
 839 *Program* 2016.
- 840 Wood, R.: *Drizzle in Stratiform Boundary Layer Clouds. Part I: Vertical and Horizontal*
 841 *Structure*, *J. Atmos. Sci.*, 62(9), 3011–3033, doi:10.1175/JAS3529.1, 2005a.
- 842 Wood, R.: *Drizzle in stratiform boundary layer clouds. Part II: Microphysical aspects*, 62(9),
 843 3034–3050, 2005b.
- 844 Wood, R.: *Stratocumulus Clouds*, *Mon. Wea. Rev.*, 140(8), 2373–2423, doi:10.1175/MWR-D-11-
 845 00121.1, 2012.
- 846 Wood, R. and Hartmann, D. L.: *Spatial Variability of Liquid Water Path in Marine Low Cloud:*
 847 *The Importance of Mesoscale Cellular Convection*, *J. Climate*, 19(9), 1748–1764,
 848 doi:10.1175/JCLI3702.1, 2006.
- 849 Wood, R., Wyant, M., Bretherton, C. S., Rémillard, J., Kollias, P., Fletcher, J., Stemmler, J., de
 850 Szoëke, S., Yuter, S., Miller, M., Mechem, D., Tselioudis, G., Chiu, J. C., Mann, J. A. L.,
 851 O'Connor, E. J., Hogan, R. J., Dong, X., Miller, M., Ghate, V., Jefferson, A., Min, Q., Minnis, P.,
 852 Palikonda, R., Albrecht, B., Luke, E., Hannay, C. and Lin, Y.: *Clouds, Aerosols, and*
 853 *Precipitation in the Marine Boundary Layer: An Arm Mobile Facility Deployment*, *Bulletin of*
 854 *the American Meteorological Society*, 96(3), 419–440, doi:10.1175/BAMS-D-13-00180.1, 2015.
- 855 Wu, P., Xi, B., Dong, X. and Zhang, Z.: *Evaluation of autoconversion and accretion*
 856 *enhancement factors in general circulation model warm-rain parameterizations using ground-*
 857 *based measurements over the Azores*, *Atmospheric Chemistry and Physics*, 18(23), 17405–
 858 17420, doi:10.5194/acp-18-17405-2018, 2018.
- 859 Xie, X. and Zhang, M.: *Improving and Understanding Climate Models: Scale-Aware*
 860 *Parameterization of Cloud Water Inhomogeneity and Sensitivity of MJO Simulation to Physical*
 861 *Parameters in a Convection Scheme* - ProQuest, search.proquest.com [online] Available from:
 862 <https://search.proquest.com/docview/1964630004?pq-origsite=gscholar> (Accessed 5 February
 863 2018), n.d.
- 864 Xie, X. and Zhang, M.: *Scale-aware parameterization of liquid cloud inhomogeneity and its*
 865 *impact on simulated climate in CESM*, *Journal of Geophysical Research-Atmospheres*, 120(16),
 866 8359–8371, doi:10.1002/2015JD023565, 2015.
- 867 Zhang, Z. and Platnick, S.: *An assessment of differences between cloud effective particle radius*
 868 *retrievals for marine water clouds from three MODIS spectral bands*, *J Geophys Res*, 116(D20),
 869 D20215, doi:10.1029/2011JD016216, 2011.
- 870 Zhang, Z., Ackerman, A. S., Feingold, G., Platnick, S., Pincus, R. and Xue, H.: *Effects of cloud*
 871 *horizontal inhomogeneity and drizzle on remote sensing of cloud droplet effective radius: Case*



- 872 studies based on large-eddy simulations, *J Geophys Res*, 117(D19), D19208–,
873 doi:10.1029/2012JD017655, 2012.
- 874 Zhang, Z., Dong, X., Xi, B., Song, H., Ma, P.-L., Ghan, S. J., Platnick, S. and Minnis, P.:
875 Intercomparisons of marine boundary layer cloud properties from the ARM CAP-MBL campaign
876 and two MODIS cloud products, *Journal of Geophysical Research-Atmospheres*, 122(4), 2351–
877 2365, doi:10.1002/2016JD025763, 2017.
- 878 Zhang, Z., Song, H., Ma, P.-L., Larson, V. E., Wang, M., Dong, X. and Wang, J.: Subgrid
879 variations of the cloud water and droplet number concentration over the tropical ocean: satellite
880 observations and implications for warm rain simulations in climate models, *Atmospheric*
881 *Chemistry and Physics*, 19(2), 1077–1096, doi:10.5194/acp-19-1077-2019, 2019.
- 882 Zhang, Z., Werner, F., Cho, H. M., Wind, G., Platnick, S., Ackerman, A. S., Di Girolamo, L.,
883 Marshak, A. and Meyer, K.: A framework based on 2-D Taylor expansion for quantifying the
884 impacts of sub-pixel reflectance variance and covariance on cloud optical thickness and effective
885 radius retrievals based on the bi-spectral method, *Journal of Geophysical Research-*
886 *Atmospheres*, 2016JD024837, doi:10.1002/2016JD024837, 2016.
- 887 Zheng, X., Klein, S. A., Ma, H. Y., Bogenschütz, P., Gettelman, A. and Larson, V. E.: Assessment
888 of marine boundary layer cloud simulations in the CAM with CLUBB and updated microphysics
889 scheme based on ARM observations from the Azores, *Journal of Geophysical Research-*
890 *Atmospheres*, doi:10.1002/2016JD025274, 2016.

891